
Probing depth enhancements of spectral domain optical coherence tomography using axicons for the inspection of additively manufactured polymer parts

P. Kumar¹, H. Martin¹, A. J. Henning¹, X. Jiang¹

¹University of Huddersfield, United Kingdom, HD1 3DH

p.kumar2@hud.ac.uk

Abstract

In the past decade, advances in optical coherence tomography (OCT) have diversified its application beyond its origins in imaging applications for the life sciences. The non-destructive nature of OCT along with its subsurface imaging capability makes it a promising tool for many industrial applications, from dimensional measurement to the inspection and characterization of materials. One such application area is in the production of additively manufactured polymer parts where OCT can provide both qualitative and quantitative feedback relating to component specification and quality. Nonetheless, one major limitation of OCT is its limited depth of focus when conventional objective lenses are used. To overcome this limitation, we used an axicon lens to achieve longer depth of focus without any degradation in the resolution. This will also simplify the measurement process and speeds up the acquisition which is very beneficial in high throughput manufacturing scenarios. We demonstrate the superior performance of axicon lens by imaging dispersed set of particles in an optical phantom, clearly showing the axicon maintaining lateral resolution over a significant depth, compared with the use of a conventional OCT. We further demonstrate the suitability of this approach for use in manufacturing applications by presenting the results of a measurement of a 3D printed microfluidic device, validated against commercial X-ray computed tomography (XCT).

Keywords: Interferometry, Manufacturing, Measuring Instrument, Polymer

1. Introduction

Recent developments in additive manufacturing (AM) processes and methods have radically enhanced manufacturing capabilities enabling the cost-efficient fabrications of optimised and customised products at a very fast rate [1]. The inherent versatility, the design flexibility of AM process and speed, it is now becoming a popular and preferred choice for manufacturing products in variety of applications ranging from automotive, aerospace, electronics, robotics, and biomedical devices [2]. Various types of materials such as metal, ceramic, composites, polymers are used for the manufacture of the parts using AM. The build process in AM is layer-by-layer deposition of the material producing a full 3D volumetric part. Any defect produced during the manufacturing process will lead to imperfections in the manufactured part. While the defects produced on the surfaces can easily be quantified, the major challenge is to evaluate defects produced within the volume of part. Imaging deeper into the sample would require special evaluation methods which can penetrate deep into the sample and create a full map of defects or voids present within. Current popular methods of inspection of additively manufactured parts are viewing by cross-sectioning or performing X-ray computed tomography (XCT). XCT is a non-invasive and a powerful tool that is even capable of imaging metal parts, but it is also expensive and slow [3].

Optical coherence tomography (OCT) is a promising non-destructive imaging technique, capable of performing subsurface imaging and reconstituting into a full 3D volumetric image of the sample [4]. In OCT, scattering signals are obtained wherever illuminating light encounters a change in the refractive

index, and the measurement of the variation of the backscattered signal is indicative of the presence of structures at different depths within the sample. Initially developed for bio-medical applications, OCT is now finding applications beyond this early usage, such as the evaluation and characterization of the various types of non-biological materials [5], inspection of ceramic materials [6, 7], reinforced polymers [8, 9], indium tin oxide conducting glass for display technologies [10], and liquid crystal displays (LCD) [11]. Wang et al. demonstrated fast and real-time inspection of the multi-photon 3D laser printed additively manufactured structures [12]. One of the limiting factors in OCT systems are their limited depth of focus when using conventional objectives. To achieve greater depth measurements either the sample or the stage is required to be scanned which complicates and slows up the measurement process. In this work we report depth of focus enhancements using an axicon lens without any degradation in resolution.

2. Theory of operation

In the present work we introduce the use of axicon lens which produces Bessel beams to enhance the depth of focus without compromising the resolution performance. Bessel beams are 'non-diffracting' beams which means the beam waist remains well maintained over a large propagation distance to an approximation [13]. True Bessel beams do not exist as they require the generation of plane waves over an infinite extent. However, for practical implementations a finite aperture Bessel beam can still produce a propagation-invariant beam waist over a much longer range compared to Gaussian beams [14]. A simple way of generating Bessel beam is to illuminate an axicon with the Gaussian beam. The intensity distribution close to the

optical axis is given by $I(r, z) = E^2(R_z)R_z 2\pi k \sin\beta / \cos^2\beta J_0^2 k_r \sin\beta$, where r is the radius of the spot perpendicular to the optical axis, β is the refraction angle of the beam after it passes through the axicon, z is position along the optical axis, k is the wavenumber of illumination source and J_0 is the zero order Bessel function. The lateral resolution is defined by the first zero of J_0 which is $r_A = 1.202 \lambda / \pi \sin\beta$. The axial range which is basically the depth of focus of the axicon lens is given by $DOF = D(\cot\beta - \tan\alpha)/2$, where D is the diameter of the illumination beam and α is the apex angle. In the case of a Bessel beam produced by an axicon of a given refraction angle β , the beam waist will remain almost constant throughout the depth of focus. When a collimated Gaussian beam (diameter- D) is focussed using a conventional objective lens (focal length- f), the lateral resolution and the depth of focus is given by $r_G = 2\lambda f / \pi D \propto NA$ and is $8\lambda f^2 / \pi D^2 \propto NA^2$ respectively. Thus, the beam waist in the case of Gaussian beam is inversely proportional to the NA of the objective lens. With higher NA, the waist decreases but the depth of focus (as defined by the Rayleigh range) decreases rapidly.

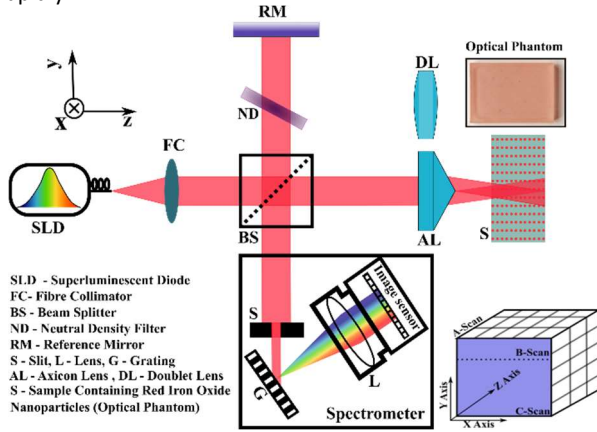


Figure 1. Schematic of the OCT apparatus

3. Methodology

The experimental setup is shown in the figure 1. Light from a broadband super-luminescent diode (SLD), Thorlabs SLD830S-A20W having the central wavelength of 830 nm and a 3 dB optical bandwidth of 55 nm is collimated using the fibre collimator generating a beam waist of 3.9 mm. The collimated beam is then split into reference and measurement arms using the beam splitter. In the reference the beam passes through a neutral density (ND) filter and reflected from the mirror placed at the end. In the measurement arm the light passes through the axicon lens (AL, Asphericon X25-200FPXB-U) or the doublet lens (DL, Thorlabs AC-080-16-B-ML) and is focussed onto the sample. For performance comparison, the lenses (AL and DL) are chosen to have approximately similar beam waist (AL- 3.734 μm , DL- 4.32 μm) at the focus point in air. The backscattered light obtained from the sample at different depths interferes with the reflected light from the reference arm, producing a spectral interferogram which is recorded by a high-resolution spectrometer (Solar Laser System S150). The spectrometer has a spectral resolution of ~ 0.06 nm over a working wavelength of 798-860 nm which enables a depth measurement range of ~ 3 mm in air. The sample is mounted onto a Newport XYZ scanning stage to obtain full 3D volumetric scan of the sample. A single point depth scan is called an A-scan. Several A-scans repeated along a line gives B-scan which when stacked together yield a full 3D volumetric scan of the sample. An XY plane extracted at a particular depth position along Z-axis is called a C-scan. The

recorded raw spectral interferometric data was processed using Fourier domain spectral analysis method [15] to obtain a spatially resolved intensity map at all scanned points. In our experimental work, we have used optical phantom, consisting of red iron oxide particles (nominal diameter 400 nm) evenly distributed in a translucent epoxy resin. The phantom provides a well-controlled sample with which to quantify and compare the imaging response of the two OCT systems under investigation, with the scattering particles being small enough to act as point scatterers by which the PSF may be estimated. In addition, a 3D printed microfluidic device was also used as a target to demonstrate the AL system operating on a real-world device.

4. Results

The 3D volumetric scan of the optical phantom was obtained by scanning it in XY directions. Figure 2 shows the matched frame C-scan image of the scatterers using the axicon and the doublet lens. A matching scatterer is shown encircled.

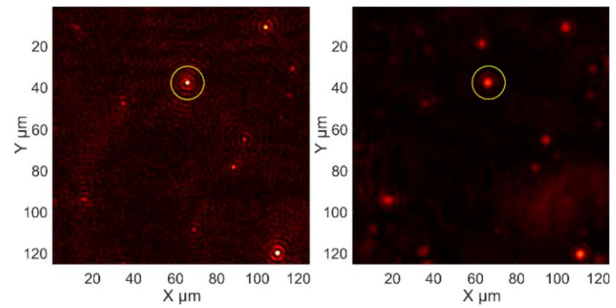


Figure 2. Matched frame C scan image of the scatterers using the axicon and the doublet lens. A matching scatterer is shown encircled.

Further volumetric scans of the optical phantom were obtained using the AL at different axial translations. An intensity thresholding approach was applied to the 3D volumetric data to automatically locate the intensity maxima, identify the individual scatterers, and generate a point cloud. Figure 3 shows point cloud representing the spread/location of scatterers at $z = 0$ and an axial translation of $z = 500 \mu\text{m}$ away from the AL.

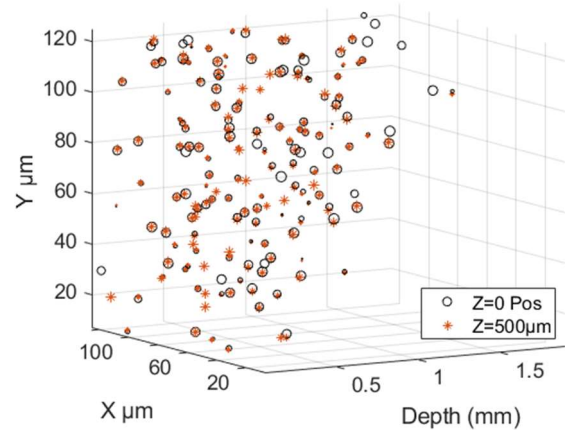


Figure 3. Point cloud representation of the scatterers at different depths using the AL.

From the above point cloud plot, it can be observed that majority of scatterers registered a location match on compensating the induced axial translation. Few individual unmatched scatterers can also be seen. This may be due to the intensity variation of the scatterers with depth, making them fall out of the threshold intensity value limit. Matching registrations

of the scatterers at different depths confirms the expected operating behaviour of the system, that is the shift in the location of a scatterer corresponds to the induced axial translation of the optical phantom away from the AL.

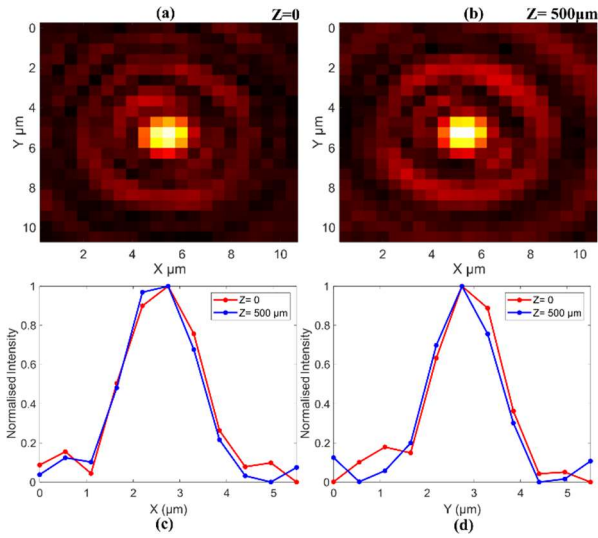


Figure 4. C Scan Image of the chosen scatterer using the AL (a), (b) and its corresponding transverse PSF response (c), (d) at $z=0$ and $z=500$ axial translation

We chose the single scatterer (encircled in figure 2) to evaluate its response at two axial depths. Figure 4(a & b) shows the C-scan image and figure 4(c & d) shows the transverse point spread function (PSF) plots shows no noticeable change in the response of the scatterers at different axial depths. The PSF data for the transverse directions had a Gaussian-fit applied prior to extracting the FWHM values. The calculated FWHM values were $1.82 \mu\text{m}$ and $1.63 \mu\text{m}$ in X and Y lateral directions respectively for the AL based system. The axial translation of the optical phantom was extended further down to 2 mm in steps of $500 \mu\text{m}$ to obtain volumetric data at each step. FWHM values from the PSF response of the scatterer were calculated at different axial translations.

Similar volumetric scans were obtained using the DL system in steps of $20 \mu\text{m}$ over a range of $120 \mu\text{m}$. Figure 5 shows the C-scan images of the scatterers for different axial translations of the optical phantom. It is clear from the figure that on either side just $60 \mu\text{m}$ away from focus, the scatterer gets completely defocused.

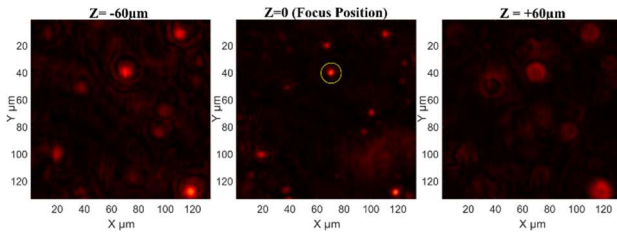


Figure 5. C scan images of scatterers at axial translations using the DL.

For the transverse and axial resolution comparisons of the AL and DL, the PSF of the same matching scatterer was tracked at different axial translations (along Z) of the optical phantom. The PSF of the chosen scatterer along the transverse directions (X and Y) at focus is shown in figure 6. The calculated FWHM value of the PSF response at the focus is $3.93 \mu\text{m}$ and $3.87 \mu\text{m}$ in transverse x and y directions respectively which correlates well with the theoretical resolution calculated to be $4.22 \mu\text{m}$.

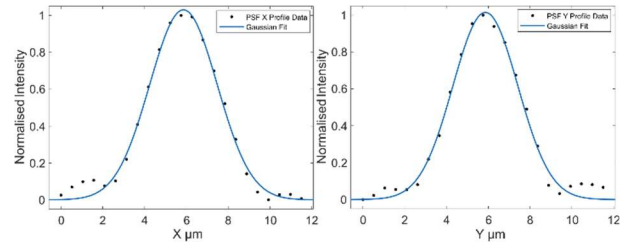


Figure 6. PSF response of the scatterer using DL at the focus position in transverse XY directions

Similarly, the axial resolution of the system for both the AL and DL was evaluated from the axial PSF data of a selected scatterer. Figure 7 shows the axial PSF plots for the axicon and the doublet lenses. The axial PSF data was Gaussian fitted and FWHM values of the chosen scatterer was calculated to be $12.93 \mu\text{m}$ for the AL and $15.31 \mu\text{m}$ for the DL. The axial resolution of system was found to be quite similar order in both the cases. This is to be expected as the axial resolution in spectral domain OCT is set primarily by the illumination wavelength range.

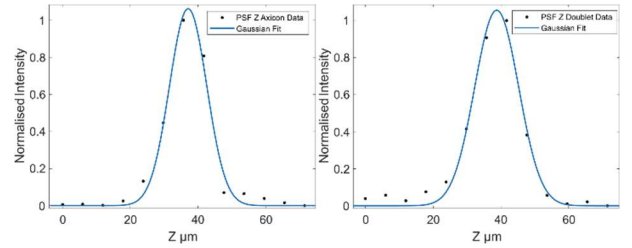


Figure 7. PSF response of the scatterer using AL and DL along axial direction

Further FWHM values for both the systems AL and DL were calculated at different axial distances. Figure 8 presents the FWHM values of the PSF response of the chosen scatterer with axial distance. It can be seen from the figure 8(a) that the AL system maintains its transverse resolution ($\sim 1.62 \mu\text{m}$ along X and $1.52 \mu\text{m}$ along Y) over a depth of 2 mm compared to the doublet where resolution starts degrading much faster just beyond its theoretical DOF limit of $35.39 \mu\text{m}$.

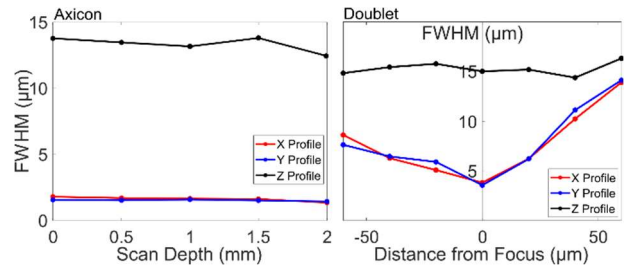


Figure 8. FWHM values in XYZ of the PSF using: (a) AL; (b) DL.

The average axial resolution at all depths obtained using the AL and the DL are $13.33 \mu\text{m}$ and $15 \mu\text{m}$ respectively. The value of the axial resolution obtained for both the axicon, and the doublet lens is higher than the theoretical value of $\sim 5 \mu\text{m}$ which can be due to the non-Gaussian light source used and the dispersion mismatch between the reference and the sample arm [14]. From the above results it is evident that the axicon exhibits superior transverse resolution and imaging performance compared to the conventional doublet lens used in OCT systems. To further investigate the imaging performance of the axicon lens, a real polymer AM sample was imaged, as shown in figure

9(a). This is a microfluidic device having an overall dimension of 10 x 6 x 2 mm, printed using an ultra-high resolution 3D printer (Microarch S130) using BIO resin. The smallest lateral channel dimensions are 18 μm and 30 μm .

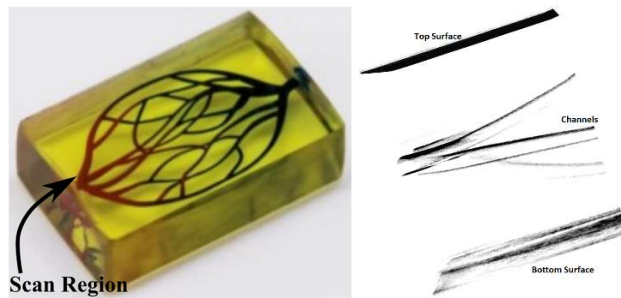


Figure 9. (a) 3D Printed blood vessel sample (b) The volumetric scan of the sample using the ALOCT

Figure 9(b) shows the volumetric measurement of the printed blood vessel model were obtained using the ALOCT (Axicon Lens Optical Coherence Tomography) system over a scan area of 1.2 x 1.2 mm with a lateral sampling interval of 1 μm . The main inlet and branching channels can clearly be seen at different depths within the scan volume. Figure 10 shows the cross-sectional B-scan image of the channel close the branching out location. The channel (L-R) sizes measured using the axicon OCT system are 198 μm , 159 μm , 225 μm and 236 μm (figure 10).

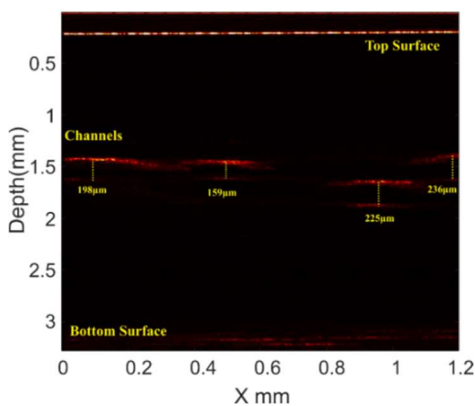


Figure 10. Cross-sectional B scan image of the 3D printed blood vessel sample obtained using the ALOCT just after the branching out. Channels L-R sizes are 198 μm , 159 μm , 225 μm and 236 μm respectively.

To validate the above measurement, the 3D printed sample was measured using a Nikon XT H225 X-Ray Coherence Tomography (XCT) system. A 3D render of the volumetric data is shown in the figure 11(a).

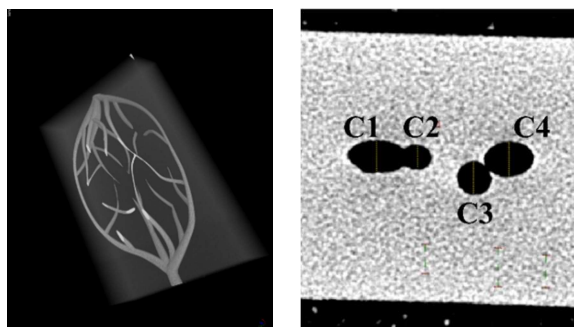


Figure 11. (a) XCT image of the 3D printed Blood Vessel Sample with the density values inverted, (b) The cross-sectional slice image of the branching out channels C1, C2, C3 and C4.

Some of the smallest channels are not resolved due to the limited resolution of the XCT. The measured values of the channels (C1, C2, C3 and C4) using the XCT just after the onset of channels branching out are found to be 226 μm , 169 μm , 236 μm , 240 μm respectively (figure 11(b)). The measurement results obtained from the ALOCT system correlates closely with the measurement obtained using the XCT. Slight variation in the calculated channels widths may be due to error in precisely locating the cross-sections within the volume, this could be improved by fabricating suitable fiducial marks within the sample volume, something that is easily achieved with the AM technique.

5. Conclusion

In this work we have presented depth of focus enhancements far beyond the conventional objective lens in an optical coherence tomography system by using an axicon lens. Greater depth of focus will allow much deeper and quicker assessment of the sample/parts by alleviating the need of multiple scans for full-depth imaging. Measurement result of the additively manufactured blood vessel sample establishes the potential usability of ALOCT for industrial metrology applications. Further work will involve improving the dispersion mismatch of the system, optimising the measurement scanning process and testing/evaluating the system on variety of samples.

References

- [1] Ngo, Tuan D. et al (2018) Additive manufacturing (3D printing): A review of materials, methods, applications, and challenges *Composites Part B: Engineering*
- [2] Pfähler, K. et al (2019) Exploring application fields of additive manufacturing along the product life cycle. *Procedia CIRP* **81** 151-156
- [3] Guan, G. et al, (2015) Evaluation of selective laser sintering processes by optical coherence tomography *Materials & Design* **88** 837-846
- [4] Schmitt, J. M. et al (1995) Subsurface imaging of living skin with optical coherence microscopy *Dermatology* **191**(2) 93-98
- [5] Stifter, D. (2007) Beyond biomedicine: A review of alternative applications and developments for optical coherence tomography *Applied Physics B* **88** 337-357
- [6] Duncan, M. D et al (1998) Subsurface defect detection in materials using optical coherence tomography *Optics Express* **2**(13) 540-545
- [7] Dunkers, J. P. et al (2001) The application of optical coherence tomography to problems in polymer matrix composites. *Optics and Lasers in Engineering* **35**(3) 135-147
- [8] Wiesauer, K. et al (2007) Investigation of glass-fibre reinforced polymers by polarisation-sensitive, ultra-high resolution optical coherence tomography: Internal structures, defects, and stress *Composites Science and Technology* **67**(15-16) 3051-3058
- [9] Yao, J. et al, (2013) Nondestructive metrology by optical coherence tomography empowering manufacturing iterations of layered polymeric optical materials *Optical Engineering*, **52**(11)
- [10] Tsai, M. T. et al (2011) Defect detection and property evaluation of indium tin oxide conducting glass using optical coherence tomography. *Optics Express*, **19**(8) 7559-7566
- [11] Kim, S. et al (2011) Nondestructive defect inspection for LCDs using optical coherence tomography. *Displays* **32**(5) 325-329
- [12] Wang, X. et al (2022) Optical coherence tomography—in situ and high-speed 3D imaging for laser materials processing. *Light: Science & Applications*, **11**(1) 280
- [13] Durnin, J. A. (1987) Exact solutions for nondiffracting beams. I. The scalar theory. *JOSA A*, **4**(4), 651-654
- [14] Durnin, J., Miceli, J. J., & Eberly, J. H. (1988) Comparison of Bessel and Gaussian beams. *Optics Letters*, **13**(2), 79-80
- [15] Wojtkowski, M. et al (2002) In vivo human retinal imaging by Fourier domain optical coherence tomography. *Journal of biomedical Optics* **7**(3) 457-463